

Miniaturized Fourier-plane fiber-scanner for OCT endoscopy

Authors

Address

E-mail: [email](#)

February 2014

Abstract.

1. Introduction

Optical Coherence Tomography (OCT) is a scanned imaging method based on the interferometric detection of very short coherence length light reflected back from the inspected tissue, providing depth-resolved information on the tissue morphology manifested as refractive index variations [1]. Furthermore, functional OCT extensions can provide complementary information on the tissue physiology without additional complexity in the imaging optics. For example, by probing the transient changes in the inspected tissue, Doppler OCT can image microvascularization in the inspected tissue, effectively performing angiography. Polarization-sensitive OCT, on the other hand, probes the optical nonlinearity of certain biological materials(e.g. collagen) providing information equivalent to higher harmonic generation microscopy [2]. Combined with its relatively large imaging depth of up to 2.5 mm, this unique versatility renders OCT a particularly important imaging modality for the emerging endoscopic optical biopsy field. However, widespread clinical application of endoscopic OCT is significantly inhibited by the lack of robust endoscopic probes not only thin enough to fit into the working channels of commercial endoscopes, but also short enough to navigate through confine spaces, such as the nasal cavity.

The first endoscopic OCT implementations were restricted to side viewing, single modality OCT catheter-endoscopes that sampled the tissue by translating [1] or rotating [2, 3] the probe to acquire *in-vivo* 2D cross sections through the lumen. This scanning method, displacing the entire catheter, resulted in poor dimmensional accuracy and speed. This can be solved by performing the scanning within the probe. Earlier works demonstrated this approach using Coherent Fiber Bundles (CFB) to create forward viewing endoscopes, where individual cores in the CFB were scanned sequentially to perform OCT imaging. The advantage of this method is that the scanning mechanism is located outside the body, which allows the endoscope tip to be relatively compact. As a tradeoff, the final image quality acquired with such systems suffered from poor signal-to-noise ratio due to the CFBs multi-mode behavior and distinct inter-core coupling [4]. Furthermore, these systems were unsuitable for flexible endoscopes due to the rigidity of CFBs. A new mechanism, the *image plane fiber scanner* [5], allowed forward-viewing video endoscopes with diameters under 1 mm within thin, flexible catheters. These devices use the concept of mechanical resonance to amplify the subtle movement of a piezoelectric actuator into a large displacement of the tip of an optical fiber oscillating in its first resonant mode. If the tip of the scanner is placed at the image plane of an optical system, as depicted in figure 1, the

lateral displacement of the fiber will image the object plane.

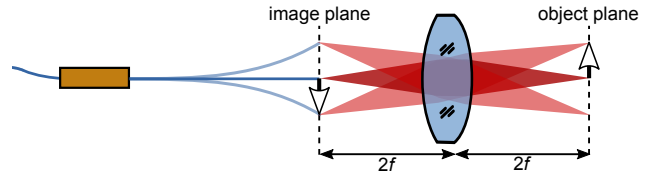


Figure 1. Working principle of an image plane fiber scanner

Although this scanning method can be extended to OCT, the high resonance frequency of the fiber, typically in the range of several kilohertz, results in very coarse spatial sampling. This effect reduces the imaging resolution drastically towards the edge of the imaging field [6]. Although it is possible to decrease the resonance frequency by using a longer fiber or a weight on its tip [7], this approach significantly increases the length of the device, rendering it unsuitable for the majority of flexible endoscopic imaging applications. In this work, we demonstrate a novel fiber scanner architecture specifically optimized for endoscopic OCT, namely the Fourier plane fiber scanner. This architecture enables shorter OCT endoscopes with higher spatial sampling with shorter rigid tip length. Furthermore, it performs telecentric scanning, which reduces vignetting in the outer areas of the image and avoids distortions in the reconstructed 3D images.

The requirements considered for the opto-mechanical design of the probe are summarized in Section 2. Optical and mechanical design details follow in Sections 3 and 4, respectively. A detailed account of the manufacturing and assembly process is provided in Section 5. Finally, in Section 6, the imaging performance of the developed systems is scrutinized in detail.

2. Design requirements

The design of a miniaturized OCT imaging probe is constrained optically by the requirements emerging from the imaging modality, and mechanically by the operation scenario and target imaging tract. From an optical perspective, the scanned imaging system should be optimized for a low numerical aperture (NA) at the object side, such that the depth-of-field (DoF) of the focused beam is several millimeters long to enable a long penetration depth (usually in the 2-4 mm range). Commonly, OCT systems are designed to have an NA between 0.02 to 0.05, depending on the specific tissue type to be measured. Since the axial resolution for OCT is only dependent on the spectral range of the light source, and the lateral resolution is of secondary importance, no specific constraint was considered in this department. In order to enable continuous video

feed provided by the accommodating endoscope system during the OCT measurement, the working distance of the probe should be larger than 5 mm. Finally, a minimum field of view of 1 mm is considered to obtain tomograms of meaningful lateral extent.

The upper limits on the physical dimensions of the probe are dictated by the compatibility with existing endoscopy equipment. If considered as an optical biopsy extension for conventional endoscopes, the probe should be thin enough to fit into the working channel, which are typically have diameters of 2.6–3.2 mm. Furthermore, in order to render the system compatible with flexible endoscopes, the rigid end length should also be smaller than 2 cm. Piezoelectric fiber scanners developed in the literature could satisfy the former requirement, but fail to provide practical scanning characteristics within the required length limit [1].

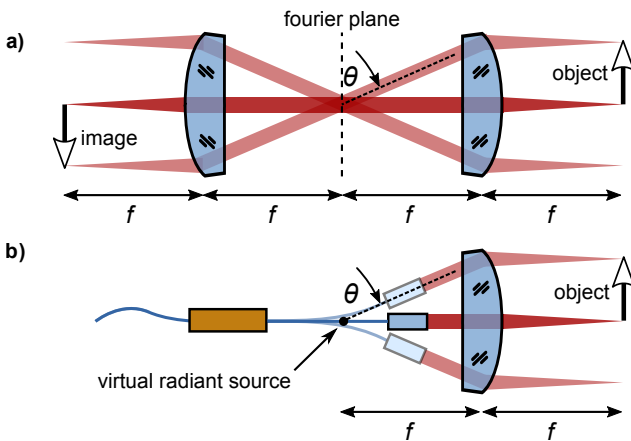


Figure 2. Working principle of the Fourier plane fiber scanner. **a)** Illustration of a classical telecentric system. The height of the object is translated into an angle θ in the collimated region between the two lenses. This angle is again translated into a corresponding image height by the second lens. **b)** Illustration of the OCT beam path using a fiber scanner in first resonance mode. The movement of the GRIN lens due to the fiber scanner and the distance between the GRIN lens and the focusing lens creating the same optical behavior as it can be observed in a classical telecentric system.

The scanner proposed in this work fulfills the above-mentioned requirements by implementing a Fourier plane fiber scanner (FPFS) architecture. Compared to the image plane fiber scanner, depicted in Figure 1, the FPFS bears a collimating GRIN lens at its tip, which also reduces the resonance frequency of the vibrating cantilever. The fiber scanner is then positioned such that the lateral and angular movement of the scanner replicates the beam angles in the collimated region of a classical telecentric $4f$ optical system, as illustrated in Figure 2. At any point of the oscillation the output beam coming from the GRIN lens points to a fixed virtual radiant source, since the

bending shape of the scanner is approximately linear with the amplitude. Thus, the ratio of the GRIN lens angle θ to its vertical displacement y is kept constant $y = d \cdot \tan \theta \simeq d \cdot \theta \Rightarrow \frac{\theta}{y} = \text{const}$, and the motion of the GRIN lens is linearly translated into the displacement of the focus spot along the image plane. Next, we discuss the design and theoretical optical performance of the FPFS implemented for this work.

3. Optical design

In a FPFS, the numerical apertures and focal lengths of the scanning and objective lens are related by the diameter of the beam in the intermediate region between both lenses. Thus, based on the schematic of Figure 3, the following geometrical optics relations are obtained: $d_{\text{beam}} \simeq 2 \cdot f_{\text{GRIN}} \cdot \text{NA}_{\text{fiber}}$ and $d_{\text{beam}} \simeq 2 \cdot f_{\text{obj}} \cdot \text{NA}_{\text{OCT}}$. By combining the two expressions, the main design equation for the scanner is obtained as

$$f_{\text{GRIN}} \cdot \text{NA}_{\text{fiber}} = f_{\text{obj}} \cdot \text{NA}_{\text{OCT}}. \quad (1)$$

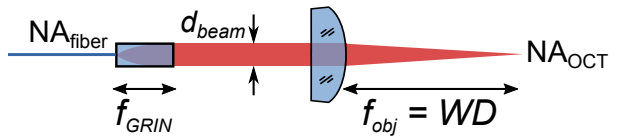


Figure 3. Optical diagram for the scanner at rest position indicating the main parameters.

Since the only commercially available single mode fiber working in the necessary wavelength range and with thinned cladding diameter (refer to section 4) is *Thorlabs SM980G80*, the optical design of the probe was optimized around the fiber characteristics. This component has a diameter of $80 \mu\text{m}$ and with $\text{NA}_{\text{fiber}} = 0.18$ at $\lambda = 1.33 \mu\text{m}$. In order to collimate the output from the fiber without clipping the gaussian beam in excess, a GRIN lens with an NA_{GRIN} higher than NA_{fiber} is needed. GRINTECH *GT-LFRL-035-024-20-CC (1550)* was chosen, with an $\text{NA}_{\text{GRIN}} = 0.20$ and $f_{\text{GRIN}} = 0.91 \text{ mm}$. This leads to a collimated beam diameter exiting the GRIN lens of $350 \mu\text{m}$.

Now, by using the relation in Equation 1 we can design $f_{\text{objective}}$ by choosing an adequate NA_{OCT} . By choosing an intermediate NA_{OCT} of 0.022, the focal length of the objective lens can be selected by

$$f_{\text{obj}} = f_{\text{GRIN}} \frac{\text{NA}_{\text{fiber}}}{\text{NA}_{\text{OCT}}} = 0.91 \text{ mm} \frac{0.18}{0.022} = 7.5 \text{ mm}. \quad (2)$$

With these parameters, the maximum field-of-view (FOV) will be limited by the aperture size of the objective lens, given that the fiber scanner can provide sufficient scanning angle. With a lens diameter of 2 mm, the maximum FOV is $1.65 \text{ mm} (d_{\text{lens}} - d_{\text{beam}})$.

3.1. Analysis of the lateral resolution

To model the complete imaging performance, the probe is first considered as an illumination device. The size of the projected spot on the image plane (illumination point spread function (PSF)) and the corresponding illumination modulation function (MTF) are given by

$$\text{PSF}_{\text{ill}}(\mathbf{r}) = \text{PSF}_{\text{core}}(\mathbf{r}M) * \text{PSF}_{\text{optics}}(\mathbf{r}) \quad (3)$$

$$\text{MTF}_{\text{ill}}(\mathbf{k}) = \text{MTF}_{\text{core}}(\mathbf{k}/M) \cdot \text{MTF}_{\text{optics}}(\mathbf{k}) \quad (4)$$

where, $\text{PSF}_{\text{optics}}(\mathbf{r})$ and PSF_{core} are the point spread functions due to optical system and the fiber mode shape, respectively. This behavior can be observed in Figure 4a, where MTF_{core} and $\text{MTF}_{\text{optics}}$ are simulated according to the design values given above. The next step considers the detection or collection of the backscattered light. If all the light coming from the fiber is projected in the PSF_{ill} , we can use the Helmholtz reciprocity property of light to state that the photons originating within this PSF will be collected by the fiber and detected by the photodiode. Thus, the detection PSF is equivalent to the illumination PSF, and the complete imaging system PSF is given by

$$\text{PSF}_{\text{sys}}(\mathbf{r}) = \text{PSF}_{\text{ill}}(\mathbf{r}) \cdot \text{PSF}_{\text{det}}(\mathbf{r}) \simeq \text{PSF}_{\text{det}}(\mathbf{r})^2. \quad (5)$$

Equivalently, the overall system MTF is written as

$$\text{MTF}_{\text{sys}}(\mathbf{k}) = \text{MTF}_{\text{ill}}(\mathbf{k}) * \text{MTF}_{\text{det}}(\mathbf{k}) \simeq \quad (6)$$

$$\simeq \text{AC}[\text{MTF}_{\text{det}}(\mathbf{k})]. \quad (7)$$

These operations are numerically calculated in Figure 4b, leading to a theoretical resolution of 23.3 line pairs/mm or 43 μm .

4. Mechanical design

The FPFS uses a piezoelectric tube actuator for the scanning of the fiber-GRIN assembly at the back focal plane of the objective lens. A piezoelectric tube is a radially polarized piezoelectric material with a single inner and four outer electrodes. If a voltage difference is applied to two opposite electrodes of the tube, one side will contract while the other will expand due to the piezoelectric effect, inducing a deflection of the tip of the tube linear with the applied voltage. In case of bipolar operation, the tip deflection Δy is estimated by [9]

$$\Delta y = V \frac{2\sqrt{2}d_{31}L^2}{\pi Dh}, \quad (8)$$

where, V is the voltage applied to each opposing electrode, d_{31} is the piezoelectric strain coefficient

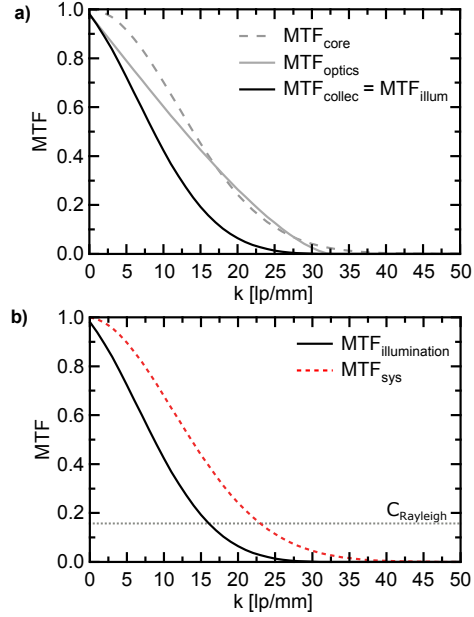


Figure 4. **a)** Simulated MTF of the illumination or collection of a single point using the proposed optical system. The MTF is limited by the finite size of the fiber core and the diffraction of the optical system. **b)** MTF of the imaging system, calculated as the convolution of illumination and detection MTFs. The theoretical resolution of such a system according to the Rayleigh contrast $C_{\text{Rayleigh}} = 0.152$ [8]) is 23.3 line pairs/mm or 43 μm .

of the material in direction perpendicular to the polarization direction, L is the length of the tube, D its outer diameter and h is the wall thickness. Thus, longer tubes with a thinner diameter and wall thickness maximize the deflection of the tip. In this work, we used a *Physik Instrumente (PI) GmbH* piezoelectric tube with 800 μm external diameter, 500 μm internal diameter and 3.7 mm length. The tip deflection of this actuator is in the order of 20 nm/V. This minute deflection can be amplified by mechanical coupling of the oscillation energy into the cantilever of the scanner formed by a optical fiber segment to which a GRIN lens is glued, as depicted in Figure 5a.

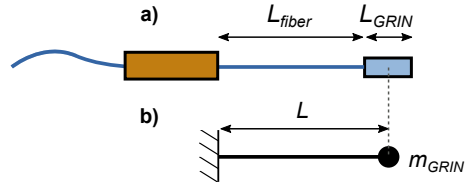


Figure 5. **a)** Schematic drawing of the piezoelectric scanner, composed of a piezoelectric tube, fiber and GRIN lens. **b)** Simplified mechanical diagram obtained by modeling the fiber as a weightless cantilever and the GRIN lens as a point mass.

The fiber-GRIN assembly can be modeled as a point-loaded, fixed-free cantilever where the weight of the GRIN lens is concentrated in its center of gravity, as represented in Figure 5b. Now, by applying the

ideal mass-spring harmonic resonator equation, the resonance frequency can be estimated as

$$f_{\text{res}} = \frac{1}{2\pi} \sqrt{\frac{K_{\text{cantilever}}}{m_{\text{GRIN}}}} \quad (9)$$

where, $K_{\text{cantilever}}$ represents the elastic constant of the fiber cantilever. Following the Euler-Bernoulli theory, the spring constant of the fiber-GRIN assembly, modeled as a point-loaded fixed-free cantilever, can be calculated as

$$K_{\text{cantilever}} = \frac{3EI}{L^3} = \frac{3\pi E_{\text{fiber}} r_{\text{fiber}}^4}{4 L^3}. \quad (10)$$

Therefore, the first natural mode frequency of the cantilever is given by

$$f_{\text{res}} = \frac{1}{2\pi} \sqrt{\frac{3\pi E_{\text{fiber}} r_{\text{fiber}}^4}{4 L^3 m_{\text{GRIN}}}}, \quad (11)$$

considering that the moment of inertia of the cylindrical fiber is given by $I_{\text{fiber}} = \frac{\pi}{4} r^4$. This resonance frequency can be reduced by increasing the cantilever length L , decreasing the radius of the fiber r_{fiber} or increasing the mass at the tip m_{GRIN} . First, by attaching the GRIN lens described in section 3 attached at the tip, the resonance frequency is reduced by a factor of 62% when compared to a bare fiber scanner. Furthermore, by choosing a fiber with a cladding diameter of 80 μm instead of the standard 125 μm , the resonance frequency can be lowered by an extra factor of 60%, as the sensitivity of the resonance frequency to the diameter of the fiber is quadratic.

When selecting the length of the scanner, there are two details to consider. First, the maximum displacement of the 350 μm GRIN lens is limited by the walls of the housing to usually a small deflection. Within that small displacement it is desirable to maximize the angular deflection of the GRIN lens, leading to a larger field of view

$$\text{FOV} = 2f_{\text{obj}} \cdot \tan \theta_{\text{max}}, \quad (12)$$

what can be achieved by using shorter fiber lengths, which oscillate with a smaller radius of curvature. This exhibits a trade-off with the density of sampling, which is improved with slower resonance frequency, achievable by using shorter fiber lengths. To balance these terms, a total scanner length of 4.5 mm was chosen, which results in a resonance frequency of 770 Hz and a maximum angular deflection of 5°.

4.1. FEA simulations

In order to validate the theoretical analysis of the previous section, a finite element analysis was performed using COMSOL. The actuator was modeled as a radially polarized piezoelectric material and the rest of the structure as fused silica. The excitation voltage is a sinusoidal symmetrical potential between

the top and bottom electrodes of the tube. Note that, as the system undergoes small deflections, it is simulated assuming linear behavior without incurring in important deviations [10]. As the first step, the resonant frequency of the system is simulated. An *Eigenfrequency* study calculates the first mode resonance at 762 Hz, which closely matches the analytical estimation of 770 Hz. The mode shape at resonance is shown in Figure 6, where it can be observed that the actuator and the base of the fiber are almost static, confirming the resonant behavior of the scanner.

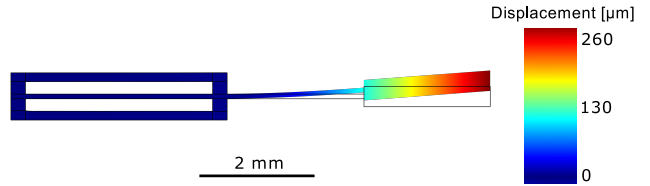


Figure 6. COMSOL simulation showing a cross section of the scanner maximum deflection at resonance for an actuation voltage of ± 75 V applied between the top and bottom electrodes. The deformed structure is color coded showing the total displacement from the rest position (shown outlined).

When using fiber scanners, the movement of the scanning fiber is limited to harmonic oscillations with a frequency close to the natural resonance at f_{res} . Therefore, the only possible 2D scan architectures are Lissajous [7] and spiral scanning. In order to simplify image reconstruction, a spiral scanning scheme is implemented in this work.

The piezoelectric tube which drives the scanner has four outer gold electrodes to control the lateral movement of the scanner, as described in section 4. Two independent voltage sources control the vertical and horizontal movement of the actuator by addressing the corresponding pair of electrodes. If sine and cosine signals of the same frequency f_{drive} are used to drive the scanner, the GRIN lens will oscillate in a circle of constant radius. If these signals are then amplitude modulated with another sinusoidal signal of frequency f_{mod} , the resultant trajectory will be a spiral, as illustrated in Figure 7.

During the full period of the spiral pattern $T_{\text{spiral}} = f_{\text{mod}}^{-1}$, two complete frames are acquired; one while the spiral grows, another while it shrinks. The whole pattern can be divided in $N_{\text{rings}} = f_{\text{drive}}/f_{\text{mod}}$ individual rings, as depicted in Figure 7. Since the tomograms are acquired in a continuous manner, the scan speed

$$v_{\text{scan}} = 2\pi r_{\text{ring}} f_{\text{drive}}. \quad (13)$$

should be sufficiently small at all times, such that the laser spot does not move more than half the PSF radius during an A-scan acquisition.

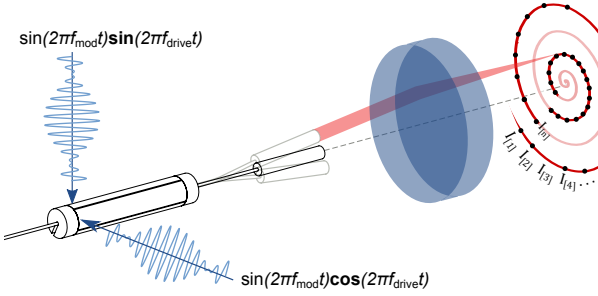


Figure 7. Schematic of the piezoelectric tube, fiber, GRIN and objective lens focusing the OCT beam (red) in a plane. The piezoelectric tube is driven with two independent amplitude modulated sine and cosine signals to generate a spiral pattern, used to acquire an image. The spiral trajectory has two different rings highlighted, where n black dots represent the sampling points of each ring. Notice that in the inner ring the sampling density is higher than in the outer one.

5. Fabrication and assembly

This section details the implementation of the probe shown in Figure 8. A polyimide ribbon cable is wrapped around the piezoelectric actuator to address its electrodes and control the lateral movement of the scanner. A single mode fiber is centered in the piezoelectric tube and the GRIN lens bonded to the tip of this fiber. This arrangement enables a compact fiber scanner with a total length of 9 mm and a resonance frequency of 750 Hz optimized for an OCT system with an A-Scan repetition rate of 100 kHz. The scanner and the objective lens are then assembled in a 3D printed polymer housing.

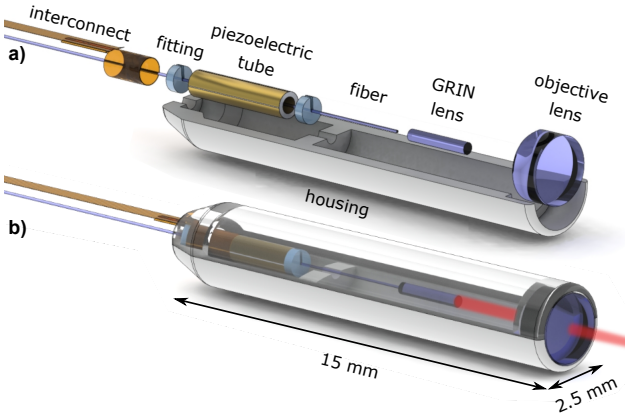


Figure 8. a) Exploded view of the components which form the OCT endoscopic probe. b) Render of the complete probe after assembly, showing the laser path pointing to the sample.

5.1. Polyimide electrodes

Due to the small diameter of the tube (800 μm), creating a reliable interface between the driving circuit

and its electrodes is not trivial. Other piezoscaner implementations use soft soldering and insulated copper wires [11–13], but the soldering process can damage the piezoelectric material, as it is exposed to temperatures above its Curie temperature and also increases the diameter of the actuator significantly, as a solder blob is needed. Instead, our design uses a polyimide ribbon cable which is wrapped around the piezo tube and addresses its four external electrodes using vias. Its geometry, cross section and application over the tube is depicted in Figure 9.

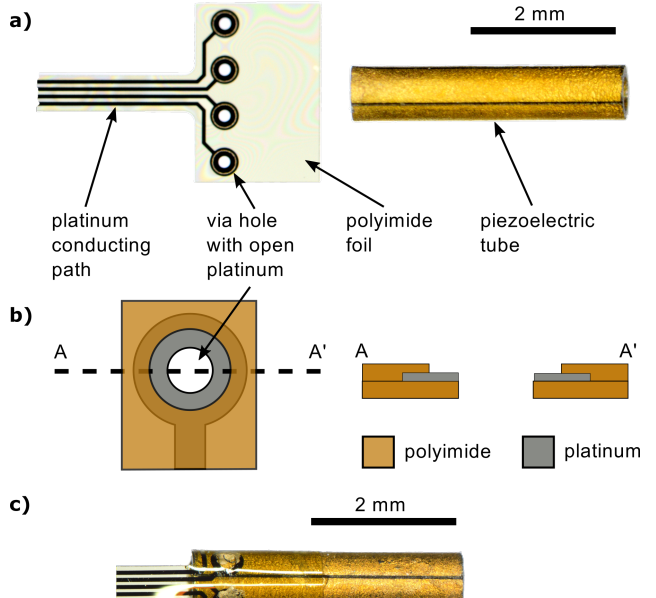


Figure 9. Polyimide electrode design. a) Left: Photo of the polyimide ribbon cable with four vias to contact the four gold electrodes of the piezoelectric tube. Right: Piezoelectric tube. b) Schematic of one via and its cross section. The platinum around the via is partly uncovered to improve the electrical connection between the cable and the piezoelectric tube. c) Photography of a polyimide ribbon cable, wrapped around the piezoelectric tube that is electrical connected through the vias by conductive glue.

The polyimide ribbon cables are manufactured using a cleanroom process summarized in Figure 10. This process is similar to the one developed for cuff electrodes for nerve stimulation [14] and consists of platinum tracks and via holes embedded in a polyimide substrate. One end of the cable is shaped to fit a zero insertion force (ZIF) connector while the other end can be rolled around the piezoelectric tube, allowing the bonding to its gold electrodes using conductive glue (Araldite 2020 with 80% wt. silver particles).

5.2. Fiber-GRIN bonding

The bonding of a single mode, 80 μm optical fiber to a GRIN lens was performed using a custom silicon

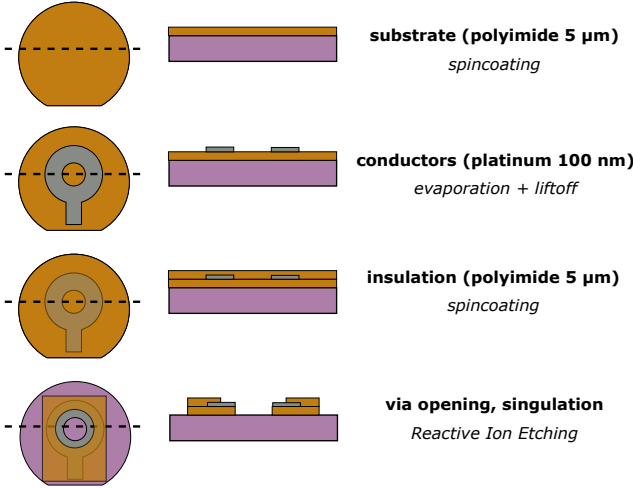


Figure 10. Simplified cleanroom processing steps for the fabrication of polyimide based electrodes in top of a silicon handling wafer. The first column shows the top view of the wafer, while the cross section is depicted in the second column.

microfabricated tool. This method allows a placement accuracy in the μm range, creating an optical and mechanical bond that operates reliably under the high mechanical stress found in a resonant scanner.

Prior OCT setups including GRIN lenses showed that they can cause problematic backreflections due to collimated incidence in the glass-air facet of the fiber. This problem was successfully avoided by a custom GRIN lens design with a 1° tilted exit facet, resulting in an optical system with total backreflections below 0.02%.

5.3. Assembly

The scanner and optical components are assembled in a 3D printed polymer structure that also acts as housing. A *B9Creator* stereolithography printer together with a custom acrylic resin achieves a lateral resolution of $30\ \mu\text{m}$.

The assembly is performed manually using the multiple alignment features of the housing. The exploded view in Figure 8 shows the placement of the components prior to assembly, followed by the final encapsulation. This process is summarized as follows:

- (i) The GRIN lens is aligned to the end of the fiber inside a micromachined silicon alignment tool and glued using index-matched optical adhesive.
- (ii) The GRIN-fiber assembly is slid through the piezotube and centered with laser cut FR-2 fittings, which are glued to the piezotube using cyanocrylate.
- (iii) The piezotube-fiber-GRIN assembly is placed in the bottom half of the housing and glued in

place using cyanocrylate with help of the alignment structures.

- (iv) The planoconvex lens is placed in the bottom half of the housing and glued using UV-curable optical glue.
- (v) The probe is closed with the top half of the housing and sealed with UV-curable glue.

A photograph of the assembled probe without the top half of the housing is shown in Figure 11.



Figure 11. Top view photograph of the assembled probe prior to encapsulation. Total length: 15 mm.

6. Experimental evaluation

6.1. Dynamic behavior of the scanner

The dynamic behavior of the scanner was measured by driving the scanner with a sweeping sinusoidal signal applied to a pair of electrodes and observing the amplitude of its oscillation using a position sensitive detector (PSD). The result, plotted in Figure 12a, shows the expected resonant behavior, but reveals two different resonant frequencies indicating that the resonant cantilever has two planes of symmetry or eigendirections with different stiffness. Close to resonance, they create a cross-plane instability in which excitation of the base of the resonator in the one eigendirection can lead to oscillations in the other eigendirection. This effect can be seen in the whirl plots of Figure 12b and was already identified in the first fiber scanner implementations [5].

In order to reduce the imaging distortions caused by whirling, the scanner operates at a working point *WP* slightly away from the resonance, but with a high enough mechanical gain to achieve the required amplitude of oscillation.

6.2. Lateral resolution

The lateral imaging performance of the probe is explored using a simple scanned imaging arrangement. Light from a $1.3\ \mu\text{m}$ laser source is sent to the probe through a circulator, which transfers the backscattered light from the sample to a photodetector. While the probe scans an object with a spiral pattern defined by the driving voltage datapoints ($\mathbf{u}_x[n], \mathbf{u}_y[n]$), the data acquisition system (DAQ) samples a stream of intensities at the photodetector $\mathbf{I}[n]$, as shown in Figure 13a. As these signals are generated

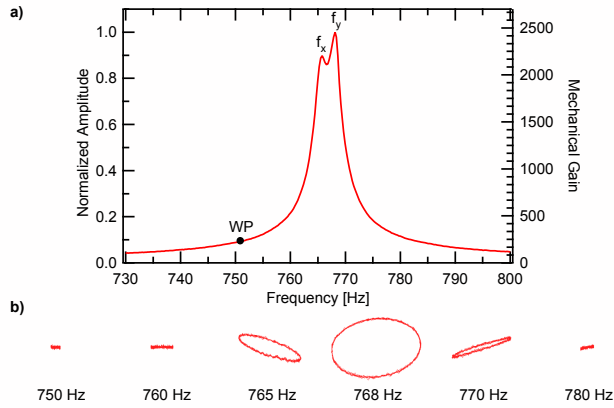


Figure 12. a) Dynamic behavior of the scanner under harmonic excitation. The two eigenfrequencies corresponding to the main axes of the scanner are marked as $f_x = 765.8\text{ Hz}$ and $f_y = 768.1\text{ Hz}$. The Working Point WP shows a gain of 220 at 752 Hz. The right axis shows the mechanical gain due to resonance, defined as the ratio of the displacement of the GRIN tip to the displacement of the piezoelectric tube tip. b) Whirl patterns obtained by exciting the scanner in the x direction with different harmonic frequencies while measuring the position of the fiber tip.

and acquired synchronously, it is expected that the recorded intensity $I[i]$ corresponds to a point in object space linearly related to the driving voltage of the piezoelectric scanner: $(x, y) = K_{\text{mech}}(\mathbf{u}_x[i], \mathbf{u}_y[i])$, where K_{mech} is a mechanical constant.

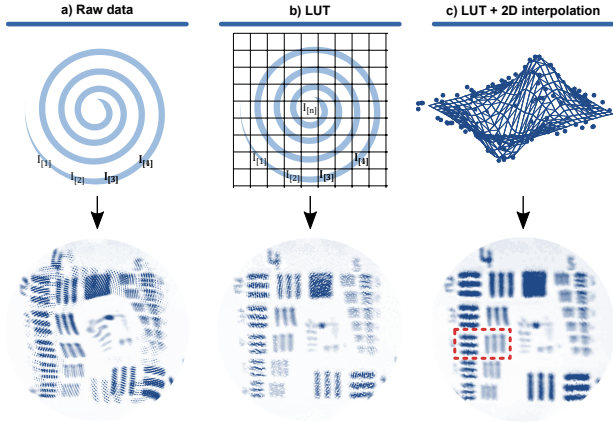


Figure 13. Different representations of the same acquired datapoints $I[n]$ of a USAF 1951 resolution test chart. The full acquired spiral consists of 374 rings of 122 datapoints, adding up to 45500 datapoints measured at 91 kHz during 500 ms. The field of view is 1.1 mm. a: Point cloud assuming ideal movement of the scanner. b: Point cloud after correcting the position of each dot using a lookup table. c: Raster image after performing a 2D interpolation from the data in d. Element 4 of group 4 of the USAF target is marked with a dashed line.

Figure 13a shows the image formed if all the datapoints $I[n]$ acquired during a full spiral are plotted as an intensity-coded dot located at the position $K_{\text{mech}}(\mathbf{u}_x[n], \mathbf{u}_y[n])$. The distortion which can be seen

in this image proves that the previous assumption of linearity is not valid. Instead, the relationship between $(\mathbf{u}_x[i], \mathbf{u}_y[i])$ and $(x[i], y[i])$ is neither linear nor simple. This is the result of whirling, as discussed in subsection 6.1. There are two general methods to overcome this problem: The first one involves closed loop operation, where the current position of the scanner is measured inside the probe and used by the plotting system to correct for the distortion [15]. The open loop alternative, used in this demonstrator, assumes that the distortion pattern is constant for a given driving signal. Then, the distorted spiral pattern $(x[i], y[i])$ can be measured after the assembly of the probe using a position sensitive device (PSD) and stored as a calibration look-up table. Once this calibration step is performed, any further frame is plotted by assigning a position $(x[i], y[i])$ to every measured intensity $I[n]$, as depicted in Figure 13b, resulting in a dot plot with less distortion. This procedure can be performed in real time. The dot plots which are obtained from spiral scanners have the inconvenient of non-uniform sampling, as can be seen in Figure 13b. Thus, to ease the further processing of the acquired images, it is beneficial to convert the non-uniform dot plot into a cartesian raster image. This can be performed by 2D interpolation, resulting in Figure 13c.

The optical performance of the scanner is qualitatively evaluated by capturing a SLI image of a USAF 1951 resolution test chart with a spiral scanning pattern. As can be seen in Figure 13c, element 4 of group 4 is resolved, indicating a resolution of 22 line pairs/mm or 45 μm . A more robust measurement of the optical resolution, independent from the scanning speed and pattern can be obtained by manually scanning the focus of the probe over a sharp chromium edge of the test chart. This way the edge spread function (ESF) is obtained. By performing a spatial derivative followed by a Fourier transform of the ESF, the MTF can be obtained, plotted in Figure 14b. Based on this curve the lateral resolution of the OCT beam path was determined at 21 line pairs/mm or 47.6 μm . This value shows a good agreement with the theoretical resolution, calculated in subsection 3.1 as 23.3 line pairs/mm or 43 μm . The 10% deviation between these values can be explained by small misalignments of the optical components induced by the process tolerances of the 3D-printed housing and the assembly process.

6.3. Depth of field measurement

The depth of field (DOF) of the OCT imaging system can be determined by measuring how much light is backreflected upon a mirror while displacing it through the z axis. The results from this experiment are plotted in Figure 15, where a full width half maximum

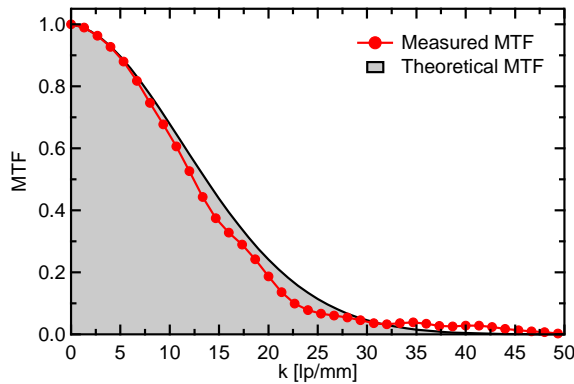


Figure 14. Experimental MTF obtained from the ESF compared with the theoretical limit using the theory from subsection 3.1.

(FWHM) DOF of 3.5 mm is calculated.

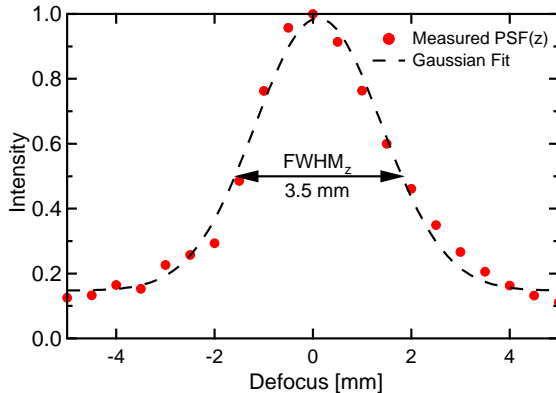


Figure 15. Measurement of the axial resolution of the single modality probe. The intensity of the light coupled back into the optical system after reflection on a mirror is plotted against the manual translation of the mirror by ± 4.5 mm from the focal plane of the probe.

6.4. OCT imaging

OCT imaging tests were performed using a swept-source OCT system at the Medical University Vienna. This system operates at a center wavelength of $1.34\text{ }\mu\text{m}$, a bandwidth of 37 nm and a theoretical axial resolution in air of $26.9\text{ }\mu\text{m}$. Using this setup, circular B-Scans of a human colon polyp and a fingertip were captured with the single modality demonstrator, shown in Figure 16.

7. Conclusion

A novel fiber scanner optimized for 3D OCT imaging is designed, implemented and characterized. The complete scanning engine has an outer diameter of

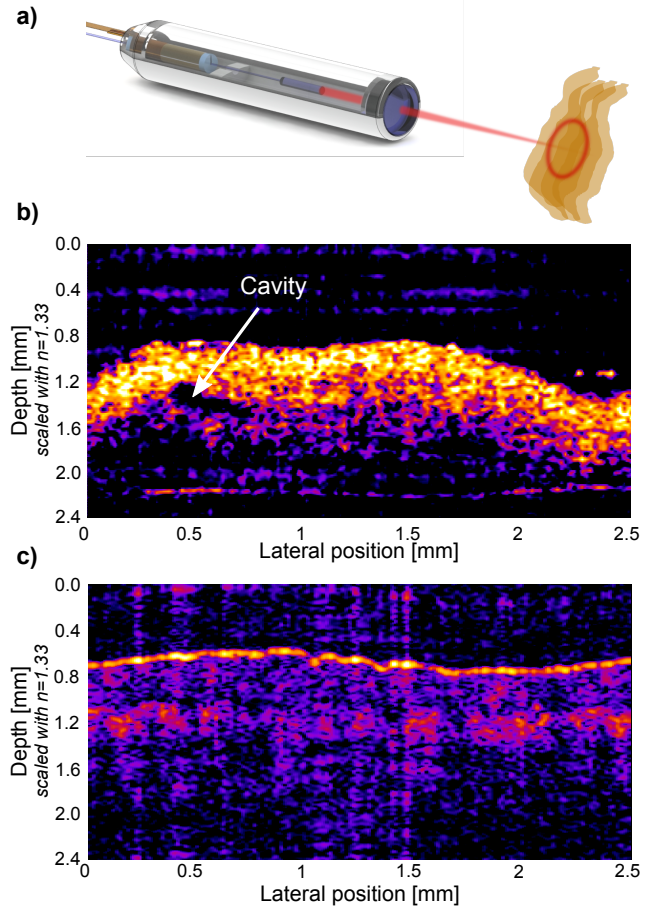


Figure 16. a) Illustration of the measurement arrangement for the circular B-Scan used as a proof of concept of OCT. b) Image of a circular OCT B-Scan of a colon polyp with a diameter $d = 0.8\text{ mm}$. Structural changes within the tissue can be detected and at the current state of the investigation the images suggest that blood vessels can be detected. c) Image of a circular OCT B-Scan of a human finger tip, where the epidermis, dermis and hypodermis can be tentatively differentiated.

0.9 mm and a length of 9 mm, and features custom fabricated $10\text{ }\mu\text{m}$ thick polyimide flexible interconnect lines to address the four piezoelectric electrodes. This scanning engine was integrated into a probe with an external diameter of 2.5 mm and a total length of 15 mm, allowing 3D OCT image acquisition over a 1 mm field-of-view and a lateral resolution of $45\text{ }\mu\text{m}$ using 1330 nm light. To the best of our knowledge, the presented demonstrator probe represents the most compact forward-looking OCT microendoscope implementation to date.

References

- [1] F. Feldchtein, G. Gelikonov, V. Gelikonov, R. Kuranov, A. Sergeev, N. Gladkova, A. Shakhov, N. Shakhova, L. Snopova, A. Terent'eva, E. Zagainova, Y. Chumakov, and I. Kuznetzova, "Endoscopic applications of optical

- coherence tomography.," *Optics express*, vol. 3, no. 6, pp. 257–270, 1998.
- [2] G. J. Tearney, M. E. Brezinski, B. E. Bouma, S. A. Boppart, C. Pitris, J. F. Southern, and J. G. Fujimoto, "in Vivo Endoscopic Optical Biopsy with Optical Coherence Tomography," *Science*, vol. 276, no. 1997, pp. 2037–2039, 1997.
- [3] G. J. Tearney, S. A. Boppart, A. E. Bouma, M. E. Brezinski, N. J. Weissman, A. F. Southern, and J. G. Fujimoto, "Scanning single-mode fiber optic catheter-endoscope for optical coherence tomography," vol. 21, no. 7, 1996.
- [4] T. Xie, D. Mukai, S. Guo, M. Brenner, and Z. Chen, "Fiber-optic-bundle-based optical coherence tomography," vol. 30, no. 14, pp. 1803–1805, 2005.
- [5] E. J. Seibel, Q. Y. J. Smithwick, C. M. Brown, and P. G. Reinhard, "Single fiber flexible endoscope: general design for small size, high resolution, and wide field of view," *EOS/SPIE European Biomedical Optics Week*, vol. 4158, no. 2001, pp. 29–39, 2001.
- [6] K. L. Lurie, A. A. Gurjarapadhye, E. J. Seibel, and A. K. Ellerbee, "Rapid scanning catheterscope for expanded forward-view volumetric imaging with optical coherence tomography," *Optics letters*, vol. 40, no. 13, pp. 3165–3168, 2015.
- [7] S. Moon, S.-W. Lee, M. Rubinstein, B. J. F. Wong, and Z. Chen, "Semi-resonant operation of a fiber-cantilever piezotube scanner for stable optical coherence tomography endoscope imaging.," *Optics express*, vol. 18, no. 20, pp. 21183–21197, 2010.
- [8] M. Blattmann, S. Kretschmer, S. Thiele, C. Ataman, H. Zappe, A. Herkommer, and A. Seifert, "Bimodal endoscopic probe combining white-light microscopy and optical coherence tomography," *Applied Optics*, vol. 55, no. 15, p. 4261, 2016.
- [9] C. J. Chen, "Electromechanical deflections of piezoelectric tubes with quartered electrodes,"
- [10] D. Fertis, "Basic Theories and Principles of Nonlinear Beam Deformations," ... and Methods to Solve Effectively Complex Nonlinear ..., pp. 1–61, 2006.
- [11] C. M. Lee, C. J. Engelbrecht, T. D. Soper, F. Helmchen, and E. J. Seibel, "Scanning fiber endoscopy with highly flexible, 1 mm catheterscopes for wide-field, full-color imaging," *Journal of Biophotonics*, vol. 3, no. 5-6, pp. 385–407, 2010.
- [12] T. Meinert, *3D-Scanner für konfokale Endomikroskopie*. PhD thesis, IMTEK, 2013.
- [13] L. Huo, J. Xi, Y. Wu, and X. Li, "Forward-viewing resonant fiber-optic scanning endoscope of appropriate scanning speed for 3D OCT imaging.," *Optics express*, vol. 18, no. 14, pp. 14375–14384, 2010.
- [14] F. J. Rodríguez, D. Ceballos, M. Schüttler, A. Valero, E. Valderrama, T. Stieglitz, and X. Navarro, "Polyimide cuff electrodes for peripheral nerve stimulation," *Journal of Neuroscience Methods*, vol. 98, no. 2, pp. 105–118, 2000.
- [15] I. L. Yeoh, P. G. Reinhard, M. C. Berg, and E. J. Seibel, "Self-Contained Image Recalibration in a Scanning Fiber Endoscope Using Piezoelectric Sensing," *Journal of Medical Devices*, vol. 9, no. 1, p. 011004, 2014.